*Article*

# Upper Ocean Response to Typhoon Kalmaegi and Sarika in the South China Sea from Multiple-Satellite Observations and Numerical Simulations

**Xinxin Yue [1], Biao Zhang [1],* , Guoqiang Liu [1,2], Xiaofeng Li [3] , Han Zhang [4] and Yijun He [1]**

[1] School of Marine Sciences, Nanjing University of Information Science and Technology, Nanjing 210044, China; yuexinxin@nuist.edu.cn (X.Y.); goqangl@gmail.com (G.L.); yjhe@nuist.edu.cn (Y.H.)
[2] Bedford Institute of Oceanography, Fisheries and Oceans, Dartmouth, NS B2Y 4A2, Canada
[3] GST at National Oceanic and Atmospheric Administration (NOAA)/NESDIS, College Park, MD 20740-3818, USA; xiaofeng.li@noaa.gov
[4] State Key Laboratory of Satellite Ocean Environment Dynamics, Second Institute of Oceanography, Hangzhou 310012, China; zhanghan@sio.org.cn
* Correspondence: zhangbiao@nuist.edu.cn

**Abstract:** We investigated ocean surface and subsurface physical responses to Typhoons Kalmaegi and Sarika in the South China Sea, utilizing synergistic multiple-satellite observations, in situ measurements, and numerical simulations. We found significant typhoon-induced sea surface cooling using satellite sea surface temperature (SST) observations and numerical model simulations. This cooling was mainly caused by vertical mixing and upwelling. The maximum amplitudes were 6 °C and 4.2 °C for Typhoons Kalmaegi and Sarika, respectively. For Typhoon Sarika, Argo temperature profile measurements showed that temperature response beneath the surface showed a three-layer vertical structure (decreasing-increasing-decreasing). Satellite salinity observations showed that the maximum increase of sea surface salinity (SSS) was 2.2 psu on the right side of Typhoon Sarika's track, and the maximum decrease of SSS was 1.4 psu on the left. This SSS seesaw response phenomenon is related to the asymmetrical rainfall on both sides of the typhoon track. Acoustic Doppler Current Profilers measurements and numerical simulations both showed that subsurface current velocities rapidly increased as the typhoon passed, with peak increases of up to 1.19 m/s and 1.49 m/s. Typhoon-generated SST cooling and current velocity increases both exhibited a rightward bias associated with a coupling between typhoon wind-stress and mixed layer velocity.

**Keywords:** upper ocean response; typhoon; satellite observations; numerical simulations

## 1. Introduction

Global warming has given rise to increased intensity of tropical cyclones in the northwest Pacific Ocean [1–3]. Typhoons are destructive tropical cyclones that periodically cause devastating weather-related natural disasters, such as flooding from intense rainfall and storm surges, which pose a growing threat to human populations and infrastructure in coastal regions [4,5]. As typhoons move over the ocean, ocean and atmosphere interactions change the storm intensity and drive energy, momentum, heat and mass exchanges. Satellite remote sensing observations, numerical simulations of the ocean and atmosphere, and a variety of in situ measurements provide a great ability to study the characteristics and mechanisms of how the upper ocean responds to typhoons. Ocean-typhoon interaction has been a cutting-edge research topic over the past few decades, and scientists have made great efforts to investigate oceanic response and feedback to typhoons.

The upper ocean's responses to a moving tropical cyclone (TC) can be divided into two stages: a forced stage and then a relaxation stage [6]. During the forced stage, strong typhoon winds induce

strong vertical mixing and upwelling, which accounts for decreased sea surface temperature (SST), increased sea surface salinity (SSS), and increased mixed layer depth. Early studies have shown that entrainment and vertical mixing are dominant mechanisms decreasing SST beneath a moving TC [7,8]. One consequence of the TC-induced large vertical shear is that the mixed layer thickness increases and entrainment becomes enhanced. Observed TC tracks and coupled ocean-atmosphere hurricane models were used to estimate the net ocean heating induced by global tropical cyclone activity, thus suggesting that TCs may play an important role in driving the thermohaline circulation [9]. It has been reported that approximately 15% of the peak ocean heat transport may be associated with the vertical mixing induced by TCs [10]. On global scale, TCs are responsible for 1.87 PW (11.05 W·m$^{-2}$) of heat transfer annually from the global ocean to the atmosphere during the passage of a storm [11].

SST response to typhoons is of particular interest because SST plays a key role in energy exchange between typhoons and the ocean. The South China Sea (SCS) is a large, semi-enclosed marginal sea, and is subject to frequent typhoons. Thus, proper characterization of typhoon-induced SST cooling may help improve understanding of typhoon mechanisms and improve typhoon intensity predictions. Previous research found that SST dropped 9 °C after the passage of Typhoon Kai-Tak and 11 °C following Typhoon Lingling [12,13]. Satellite measurements and three-dimensional numerical simulations have shown that typhoon-induced decreases in SST depend strongly on the typhoon's maximum surface wind speed, translation speed, and size [14,15]. SST cooling amplitude also strongly depends on depth of the mixed layer and thermocline stratification prior to the storm [16,17]. During strong typhoons (greater than or equal to category 4), the subsurface warming expected from vertical mixing is comparable in magnitude to the near-surface cooling; however, for weak typhoons (less than or equal to category 3), only surface cooling occurs, thus suggesting that air-sea heat exchange and vertical advection possibly play an important role in the case of weak typhoons [18]. Rapid intensification occurs when a TC pass over warm eddies owing to the increasing ocean heat content, while storm-induced mixing and SST cooling are suppressed by the warm ocean features. Composited advanced very-high-resolution radiometer observations and buoy measurements showed SST decreases of only about 0.5 °C–1 °C when Hurricane Opal passed over a warm core ring in the Gulf of Mexico [19]. In addition, when Typhoon Maemi, a category 5 storm, encountered a warm ocean eddy in the western North Pacific, there was an analogous SST cooling of approximately 1 °C [20]. Typhoon Maemi's self-induced SST cooling was suppressed by a thicker upper ocean mixed layer in the warm eddy. This prevented cold water from the deep ocean from being entrained into the upper ocean mixed layer. Moreover, the near-surface barrier layer also suppressed the typhoon-induced upper ocean cooling, leading to temperature changes that were smaller than expected [21]. When typhoon-induced forcing is strong enough to break through the barrier layer base into the thermocline, the barrier layer reduces the cooling magnitude [22].

Upper ocean current response to typhoons in the northwestern Pacific Ocean has been characterized through analysis of ocean current observations from Surface Velocity Program (SVP) drifters and Joint Typhoon Warning Center (JTWC) best track data. Near-surface current speeds greater than 2 m/s were observed during major typhoons, with strongest mean currents to the right of the storm track [23]. SVP drifter observations showed a maximum mixed layer current velocity of 2.6 m/s for Typhoon Maon [24]. Furthermore, the investigation also demonstrated that current velocity in the mixed layer depended on both the typhoon's translation speed and its intensity scale. For a slow-moving and super strong typhoon, the maximum mixed layer current velocity is roughly twice that of a fast-moving and weak typhoon. Typhoon-induced near-inertial motions are dominant during the relaxation stage, and barotropic subinertial waves and baroclinic near-inertial oscillations were both observed at this time, indicating a subinertial wave period of 2.8–4.1 days [25]. Near-inertial oscillations decayed more rapidly in shallow water than in the deep ocean, which emphasized the importance of frictional effects for characterizing responses to typhoon forcing in the shallow ocean [26].

Upper ocean current responses to typhoons have been investigated using numerical simulations and in situ observations. Strong near-surface current with maximum speed of 1.5 m/s was

observed on the right side of the track of Typhoon Kalmaegi by Acoustic Doppler Current Profilers (ADCP) [27]. This rightward bias in the surface current response can be attributed to coupling between typhoon wind-stress and mixed layer current velocity [7]. Numerical simulations suggested that typhoon-induced cyclonic currents flowed in a roughly circular pattern around a mesoscale cold eddy, with a maximum velocity of 2.5 m/s [28]. Moreover, previous research revealed that strong near-inertial rotating currents with maxima of approximately 1–1.4 m/s were induced in the mixed layer by the passage of Hurricane Gilbert [29]. Typhoon-generated near-inertial currents associated with surface cooling and deepening of the mixed layer also showed this rightward bias, with peak magnitudes of up to 0.6 m/s [7,30].

Salinity plays a significant role in upper ocean typhoon response. Observations from Argo profiling floats showed that a deepening of the mixed layer and cooling showed a significant rightward bias, whereas salinity decreased to the left of the typhoon track and increased to the right [31]. Moreover, Argo salinity profile measurements of typhoons in the western North Pacific Ocean have shown decreasing salinity 70–80 m beneath the surface to the left and right of typhoon tracks [32]. Instruments on an underwater glider also observed changes in upper ocean salinity before, during, and after the passage of Hurricane Gonzalo, showing that wind-forced mixing caused a 0.6 psu salinity increase at depths above 20 m and a 0.4 psu salinity decrease between 20 m and 130 m deep [21]. Both three-dimensional numerical simulations and in situ observations have revealed that salinity anomalies generally show a three-layer vertical structure, with the surface layer becoming cooler and saltier, the subsurface layer becoming warmer and fresher, and the lower layer becoming cooler and saltier again [22]. Although Argo floats and underwater gliders can measure upper ocean salinity, they provide scarce salinity observations on both sides of typhoon track.

Our main goal is to improve the understanding of upper ocean responses to typhoon force winds. To accomplish this, we assessed ocean conditions (SST, near-sea surface currents, and SSS) before (pre-storm), during, and after (post-storm) the passage of Typhoons Kalmaegi and Sarika in the SCS. Our assessment used synergistic multi-platform satellite remote sensing observations, numerical simulations, and in situ measurements. Satellite observations revealed sea surface typhoon responses, such as significant SST decreases and increases in near-surface current velocity. Typhoon-induced SSS variabilities were first quantified using spaceborne L-band radiometer observations. Both in situ (Argo, Conductivity Temperature Depth (CTD), and ADCP) measurements and numerical simulations showed complex subsurface responses. We further compared CTD-measured temperatures and ADCP-measured current velocities with temperatures and current velocities simulated by a three-dimensional oceanic numeric model. We used these comparisons to evaluate model performance in simulating upper ocean response during a typhoon. We also discuss some potential mechanisms of upper ocean response to typhoon.

The remainder of this paper is organized as follows. In Section 2, the dataset used in this study and methodology are described. In Section 3, the results and discussions are presented. The conclusions are given in Section 4.

## 2. Dataset and Methodology

### 2.1. Multiple-Satellite Remote Sensing Data

#### 2.1.1. Sea Surface Temperature (SST)

In this study, we used microwave optimally interpolated (OI) SST data to study typhoon-induced cooling of the sea surface. These data were provided by Remote Sensing Systems (data available at www.remss.com). The SST data were produced using observations from the Tropical Rainfall Measuring Mission Microwave Imager (TMI), the Advanced Microwave Scanning Radiometers for the Earth Observing System (AMSR-E and AMSR2) satellites, and the WindSat polarimetric radiometer aboard the Department of Defense Coriolis satellite. The ability of microwave radiometers to measure SST through clouds provided a valuable global SST map. The data were enhanced with interpolation to

fill areas missing due to orbit transition and other environmental factors, achieving a 0.25° resolution (~25 km). All OI SST values use a diurnal model to create the foundation SST for representing a noon temperature.

### 2.1.2. Sea Surface Salinity (SSS)

The Soil Moisture Active Passive (SMAP) satellite was launched in January 2015. Although SMAP was designed to measure soil moisture, its L-band radiometer can also be used to measure SSS. The SMAP has a high spatial resolution of 40 km and a wide swath of 1000 km that allows for global coverage in three days, with an eight-day repeat cycle. The Aquarius mission provided global maps of SSS with 150 km resolution on a monthly timescale. The finer spatial resolution of the SMAP makes it noisier than Aquarius, but the noise is reduced by the temporal averaging of the data over days or weeks. Therefore, SMAP provides only eight-day running mean and monthly SSS product. Remote Sensing Systems processed SMAP SSS data as Level 2C, Level 3 8-day running, and Level 3 Monthly data [33], which are available at www.remss.com. The Level 3 SSS product is gridded at 0.25° × 0.25°. In this study, we used SMAP Level 3 8-day running SSS data to analyze salinity changes before and during typhoon passage.

### 2.1.3. Rainfall Rate

We analyzed typhoon-induced rainfall using rainfall rates from WindSat and Global Precipitation Measurement (GPM) satellite observations. WindSat brightness temperatures acquired at 18.7, 23.8, and 37.0 GHz were used to retrieve rainfall rates. The daily files consisted of WindSat daily rainfall rate measurements mapped to a 0.25° × 0.25° grid, complete with data gaps between ascending and descending orbits, via the Remote Sensing Systems website (www.remss.com). For GPM, we used Integrated Multi-satellite Retrievals for GPM (IMERG) rainfall rate products (https://pmm.nasa.gov/data-access/downloads/gpm). IMERG is a Level-3 algorithm intended to intercalibrate, merge, and interpolate all available passive microwave (PMW) estimates from the GPM constellation (e.g., GMI, TMI, SSMIS, AMSR2, and MHS), using PMW-calibrated infrared estimates and rain gauge observations. IMERG rainfall rate data have spatial and temporal resolutions of 0.1 degree and 30 min, respectively.

### 2.1.4. Sea Surface Height Anomalies (SSHA) and Geostrophic Velocity Anomalies (GVA)

The altimetry products of the SL-TAC multi-mission altimeter data processing system are distributed by the Copernicus Marine and Environment Monitoring Service (CMEMS). The system processed SSHA and GVA using observations from all the following altimeter missions: Topex/Poseidon (T/P), Environmental Satellite (ENVISAT), Geosat Follow-On (GFO), European Remote Sensing satellites (ERS-1 and ERS-2), Jason-1, Jason-2, Jason-3, Sentinel-3A, HY-2A, Saral/AltiKa, and Cryosat-2. The gridded SSHA and geostrophic velocity anomaly products have spatial resolution of 0.25° × 0.25° and temporal resolution of one day. For Typhoon Kalmaegi, we focus on the 6 (pre-storm) and 16 (post-storm) SSHA and GVA in September 2014, while for Sarika, we focus on the 8 (pre-storm) and 18 (post-storm) anomalies in October 2016.

### 2.2. In Situ Observation Data

### 2.2.1. Current Velocity Profiles

To investigate upper ocean typhoon responses, we deployed a cross-shaped observational array consisting of five moored buoys and four subsurface moorings organized into five stations in the SCS. As an example, Figure 1 shows the design of Station 4, which consisted of a buoy and a mooring. Observed variables included standard meteorological parameters, ocean surface waves, currents at depths from 0 to 850 m, and temperature and salinity measurements from 0 to 400 m and near the ocean bottom. We focused on the upper ocean response to typhoons from 0 to 100 m, thus mooring-measured

datasets were not used. Stations 1 and 4 were located on the right of the track of Typhoon Kalmaegi, whereas Station 2 was on the left. All these stations were located within the maximum wind radius of Kalmaegi. Station 2 is much closer to the track than stations 1 and 4. Currents were measured using ADCP at each station: a 150 kHz (Stations 1 and 2) or 300 kHz (Station 4) downward-looking ADCP binned at 8-m (Stations 1 and 2) or 4-m (Station 4) intervals with the first bin at either 14 m (Stations 1 and 2) or 8 m (Station 4) and the last bin at either 246 m (Stations 1 and 2) or 124 m (Station 4) below the surface. The 75 kHz ADCP velocity accuracy is 1% of water velocity relative to the ADCP $\pm 0.01$ m/s, and the 150 and 300 kHz ADCP accuracies are $1\% \pm 0.005$ m/s and $0.5\% \pm 0.005$ m/s, respectively.
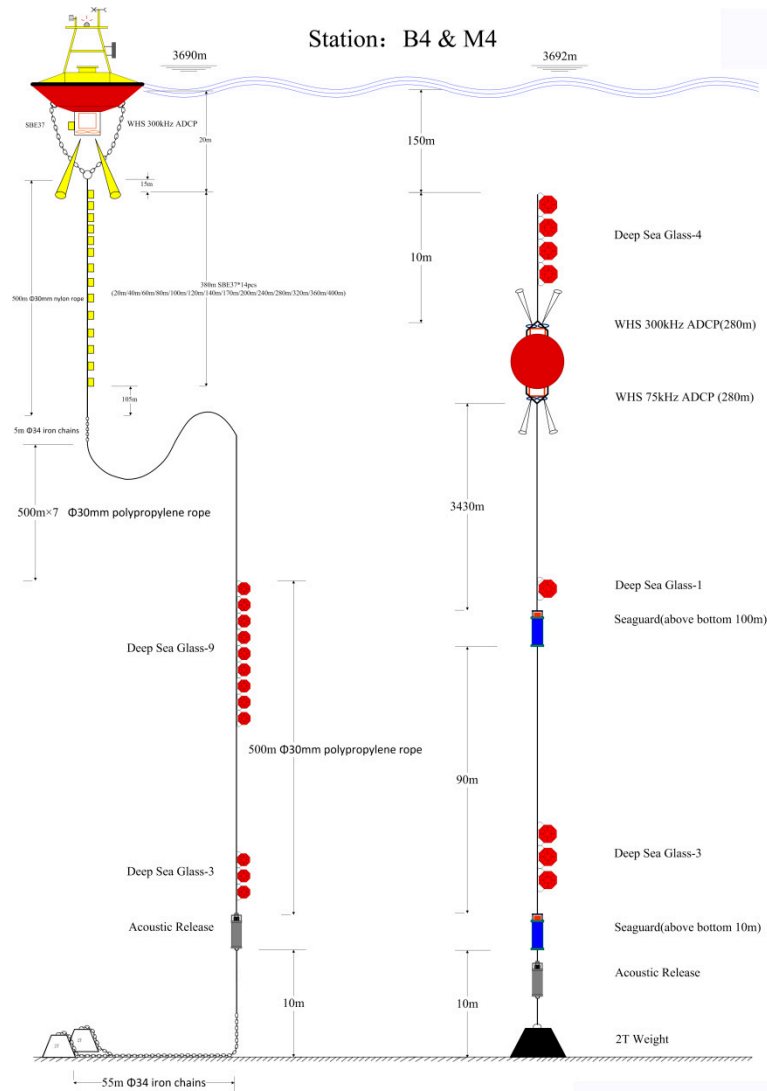


**Figure 1.** Buoy and mooring design at Station 4.

### 2.2.2. Temperature and Salinity Profiles

Argo is an array of 3887 active profiling floats, distributed almost uniformly across the global ocean, that provide temperature and salinity profiles from the surface to 2000 m deep. The array has approximately one float for every 3° of latitude and longitude and provides a new profile every 10 days. Overall, Argo provides accurate and comprehensive measurements of changes to ocean temperature and salinity, enabling systematic assessments of the physical state of the upper ocean. In this study, we used Argo temperature and salinity profiles along with CTD-measured temperature and salinity profiles to explore the oceanic impacts of Typhoons Kalmaegi and Sarika. The temperature

and salinity profiles of Typhoon Kalmaegi were measured every 2 min by CTD recorders from 0 m to 400 m placed at 20 m intervals. The CTD accuracy is ±0.002 °C for temperature and ±0.0003 S/m for electrical conductivity. There were no temperature and salinity data from Station 1 because its string of CTD recorders was lost. In addition, we extracted the Argo float profiles from the real-time quality-controlled Argo database of the China Argo Real-time Data Center (http://www.argo.org.cn). Vertical profiles from Argo floats 5904562 and 5904746 allowed us to investigate the ocean's responses to typhoons. The temporal window for the pre-storm Argo profile is 4 days before the storm and the post-storm Argo profile is also 4 days after storm passage. The differences in the locations of the pre-storm, storm and post-storm Argo profiles are within 0.11°–0.18°, and the horizontal distance can minimize the influences of background signals. The distances of Argo floats 5904562 and 5904746 are 158.5 km and 155.6 km relative to the center of the storm track, respectively.

### 2.3. Ocean Model Setup

We used the three-dimensional-ocean model, Regional Ocean Modeling System (ROMS), to numerically investigate upper ocean responses to Typhoons Kalmaegi and Sarika in the SCS. The ROMS model is a free-surface, hydrostatic, primitive equation ocean model extensively used in estuarine, coastal, and basin-scale research applications (http://www.myroms.org) [34–36]. The air–sea interface boundary Momentum and buoyancy fluxes are parameterized using the Coupled Ocean-Atmosphere Response Experiment (COARE) 3.0 bulk-flux formation [37,38], and we used the K-profile parameterization (KPP) mixing scheme detailed in [39] for vertical turbulent mixing. The KPP model has shown a reasonable level of accuracy in simulating typhoon-induced mixing [40].

The domain used in the ROMS model covers part of the SCS (14°N–23°N, 111E°–119°E). To obtain the fine oceanic structure in the region, a high resolution horizontal grid is applied ~1/32° (≈3 km). The domain has 72 terrain-following vertical levels with 0.5–2.7 m vertical resolution in the upper 100 m and then 11.5–426.1 m resolution in the interior ocean. The grid dimensions (latitude, longitude, and depth) are 271 × 304 × 72. The internal mode time step is 20 s, while the external mode time step is around 0.3 s, hourly outputs are stored for case studies. The bathymetry for the domain is taken from ETOPO2 gridded dataset, and the slop parameter is 0.2.

We obtained atmospheric forcing conditions from Climate Forecast System Version 2 (CFSv2; http://cfs.ncep.noaa.gov), a global high-resolution atmospheric hind-cast model. This version has been upgraded in respect to nearly all aspects of the system's data assimilation and forecast model components [41]. CFSv2 provides air temperature, rainfall, and humidity, which determine the atmosphere-ocean buoyancy (heat and freshwater) fluxes, and far-field pressure and wind vectors.

The initial and lateral open boundary conditions for temperature, salinity, and current were obtained from the Hybrid Coordinate Ocean Model (HYCOM), with a 1/12° spatial resolution (http://tds.hycom.org) [42]. The choice of model used for initial and boundary conditions was largely based upon data availability in this study region.

## 3. Results and Discussion

We analyzed ocean surface and subsurface physical responses to Typhoons Kalmaegi and Sarika using multiple-satellite observations, in situ measurements, and numerical simulations. Figure 2 illustrates the lifespans of Typhoons Kalmaegi and Sarika. Typhoon Kalmaegi was generated at 12:00 UTC on 10 September 2014 in the western North Pacific Ocean. It then crossed the Philippines with a 33.4 m/s maximum sustained wind speed and a 974 mb minimum sea-level pressure at 00:00 UTC on 15 September 2014. It moved northwestward and gradually decayed after making landfall. Typhoon Sarika formed as a tropical depression at 06:00 UTC on 13 October 2016 near 13°N, 130°E, traveling northwestward and reaching typhoon strength at 18:00 UTC on 14 October 2016. As Typhoon Sarika made landfall in the Philippines, it reached a maximum sustained wind speed of 59.1 m/s. The storm subsequently weakened after passing over the Philippines and moved toward the SCS, gradually decaying after making landfall over Hainan Island.
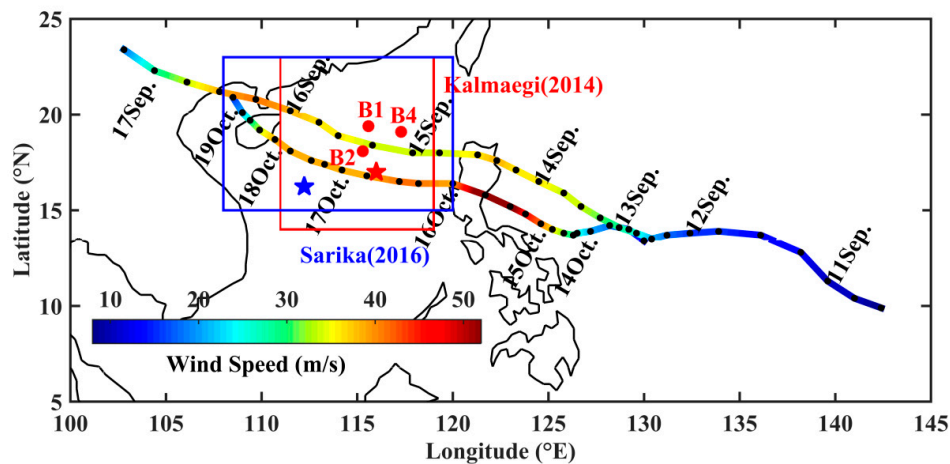
**Figure 2.** Best track of Typhoons Kalmaegi (2014) and Sarika (2016) from the Joint Typhoon Warning Center. Buoy array positions are marked by red dots (B1, B2, and B4). The red and blue stars denote the positions of Argo floats 5904562 and 5904746. The red and blue boxes mark the focused regions of the Typhoons Kalmaegi (2014) and Sarika (2016). The color bar shows maximum sustained wind speed (m/s), which indicates typhoon intensity.

### 3.1. Temperature Response

Figure 3 shows SST evolution during the passage of Typhoon Kalmaegi from 13 September to 17 September 2014. Before Kalmaegi's arrival, the SCS was characterized by warm SSTs predominately greater than 30 °C (Figure 3a). Typhoon Kalmaegi entered the SCS at 18:00 UTC on 14 September (Figure 3b), and decreased SST as shown in Figure 3c. As it moved to the northwest, Typhoon Kalmaegi induced significant SST cooling on 16 September, with a minimum SST of 24.5 °C found at the center (20.4°N, 114.3°E) of the cold pool (Figure 3d). After Typhoon Kalmaegi's departure, SST gradually recovered (Figure 3e). Figure 3f shows the SST changes between 16 September and 14 September, with SST cooling occurring from 15°N to 21°N and 113°E to 117°E. SST dropped as much as 6 °C compared to conditions prior to the typhoon (30.5 °C). Figure 4 shows a similar SST cooling phenomenon for Typhoon Sarika. Figure 4c shows large patches of cool water ranging from 25.2 °C to 27.3 °C, and a 2.7 °C drop compared with the initial stage on 16 October 2016. Over the following days, the cooled patch increased in size and grew along the typhoon track (Figure 4d). Figure 4f shows a maximum SST decrease of 4.2 °C. Both satellite observations and three-dimensional numerical simulations revealed that typhoon-produced SST cooling strongly depends on the typhoon's characteristics, such as intensity as measured by its maximum surface wind speed, translation speed, and size [14,15]. The minimum SST related to Typhoon Kalmaegi appeared on 16 September 2014 and the minimum for Typhoon Sarika occurred on 18 October 2016. The maximum wind speeds and translation speeds of these storms were 36 m/s and 38.5 m/s and 5.8 m/s and 6.9 m/s, respectively.

We estimate the vertically integrated ocean heat content (OHC) with Equation (1),

$$\text{OHC} = \rho_0 C_P \iiint \Delta T \, T dh dx dy \qquad (1)$$

where $\rho_0$ and $C_P$ are the density and heat capacity of sea water, respectively, $\Delta T$ is the magnitude of the temperature anomaly between pre- and post-storm, h is the depth of temperature anomaly extends, and x and y are the meridional and the zonal extends, respectively, of the storm-induced temperature anomaly. For all calculations, $\rho_0$ and $C_P$ are constant and equal to 1025 kg/m$^3$ and 4200 J/kg$^{-1}$·°C$^{-1}$, respectively. The depth of vertical mixing (h) is assumed as a constant and it equals to 200 m. The OHC variations between the pre- and post-storm for Typhoons Kalmaegi and Sarika are shown in Figure 5b,d. After Typhoon Kalmaegi passage, the maximum ocean heat loss was

$1.6 \times 10^8$ J/m$^2$ (Figure 5b), which is corresponding to the significant SST cooling of 6 °C (Figure 3f). For Typhoon Sarika, however, the ocean heat loss was only $0.5 \times 10^8$ J/m$^2$ (Figure 5d) and the SST drop was 4.2 °C (Figure 4f). The amplitude of SST cooling and OHC decrease owing to Typhoon Sarika is less than that of Typhoon Kalmaegi because Typhoon Sarika passed through a cold cyclone eddy (Figure 5c). Therefore, the pre-storm oceanic conditions also affect the upper ocean response to typhoons.
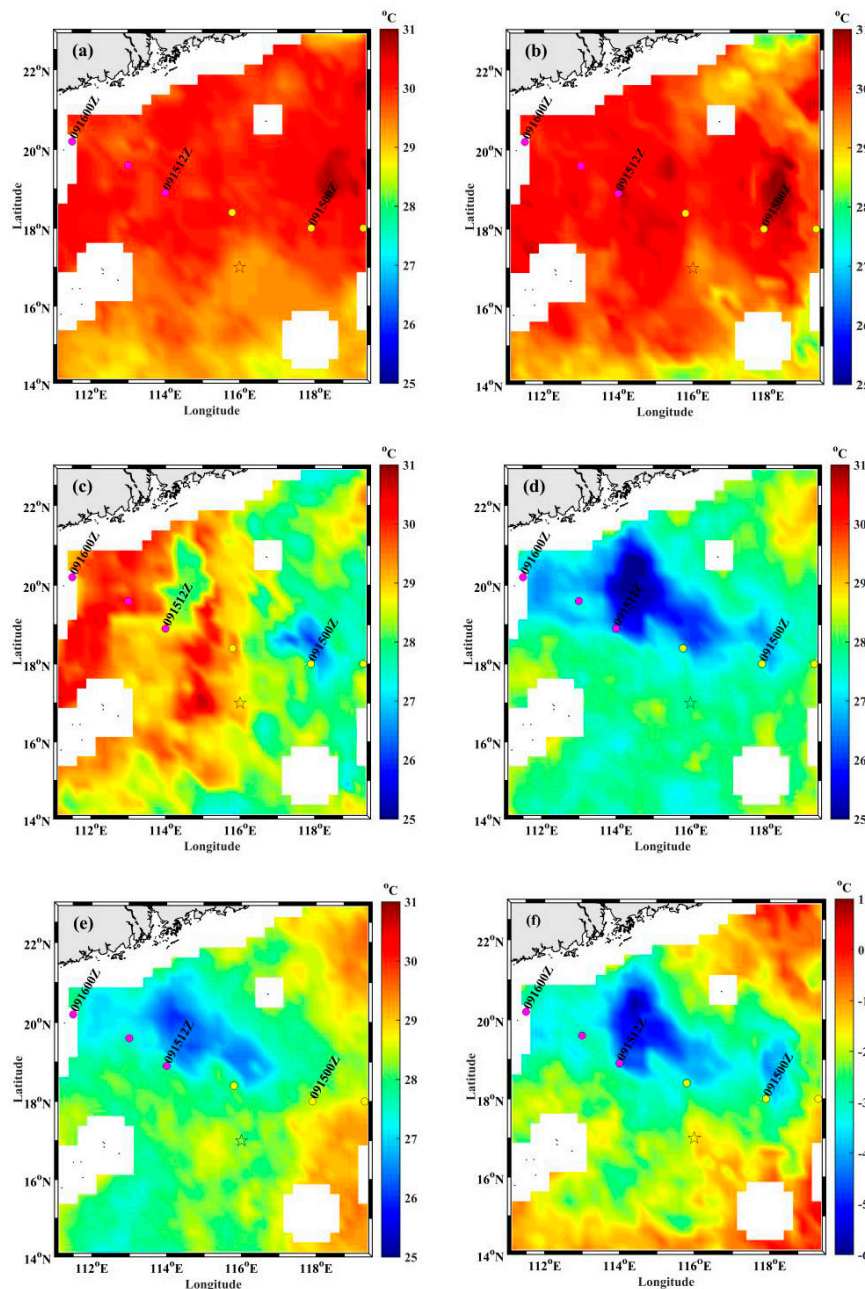


**Figure 3.** Microwave optimally interpolated SST data showing SST as Typhoon Kalmaegi passed: (**a**) on 13 September 2014; (**b**) on 14 September 2014; (**c**) on 15 September 2014; (**d**) on 16 September 2014; and (**e**) on 17 September 2014. (**f**) SST difference between 16 and 14 September 2014. The color bar denotes the temperature, in units of °C. The colored circles mark the location of the typhoon center at different times, and the colors represent the maximum sustained wind speed (m/s): yellow for 31–35 m/s and magenta for 36–40 m/s. The black star marks the position of Argo float 5904562.
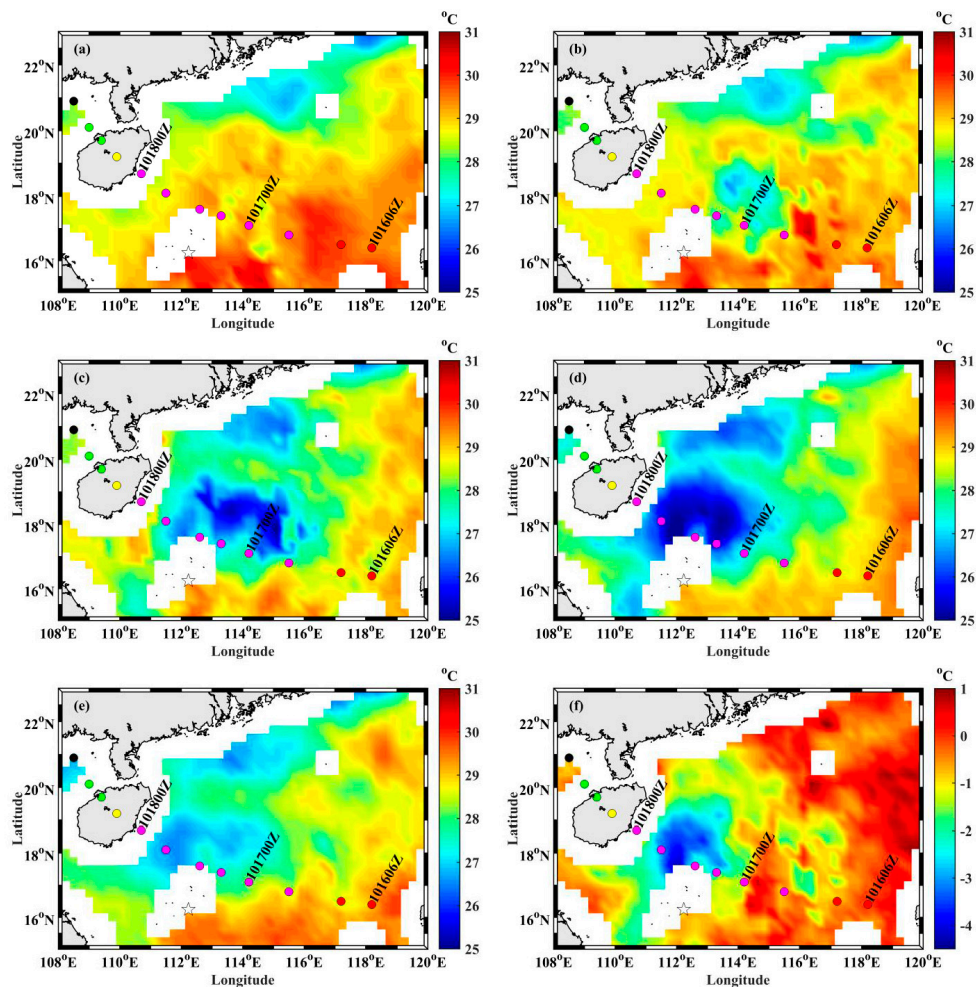
**Figure 4.** Microwave optimally interpolated SST data showing SST as Typhoon Sarika passed: (**a**) on 15 October 2016; (**b**) on 16 October 2016; (**c**) on 17 October 2016; (**d**) on 18 October 2016; and (**e**) on 19 October 2016. (**f**) SST difference between 18 and 16 October. The color bar denotes the temperature, in units of °C. The colored circles mark the location of the typhoon center at different times, and the colors represent the maximum sustained wind speed (m/s): black for <20 m/s; green for 20–30 m/s; yellow for 30–35 m/s; magenta for 35–40 m/s; and red for >40 m/s. The black star marks the position of Argo float 5904746.

Figure 6 shows SST variations that were induced by Typhoons Kalmaegi and Sarika on the left and right sides of the track. The maximum SST cooling for Typhoons Kalmaegi and Sarika occurred on the right side of the track, with corresponding locations of 39.7 km and 66.2 km from the storm center, respectively. These two locations were within the maximum wind radius, which was 113.9 km for Typhoon Kalmaegi and 138.9 km for Typhoon Sarika. We estimate the power spectral density of wind speed and mixed layer current velocity at the maximum cooling position on the right side of the typhoon. As shown in Figure 7, the peaks of power density agree well between the typhoon wind forcing and mixed layer current at the near inertial frequency. We found that a rightward SST bias occurred in the satellite observations, which is consistent with previous studies. It is mainly caused by the fact that the storm wind-stress vector turns clockwise over time on the right side of the track, and was roughly resonant with mixed layer current [7,43].
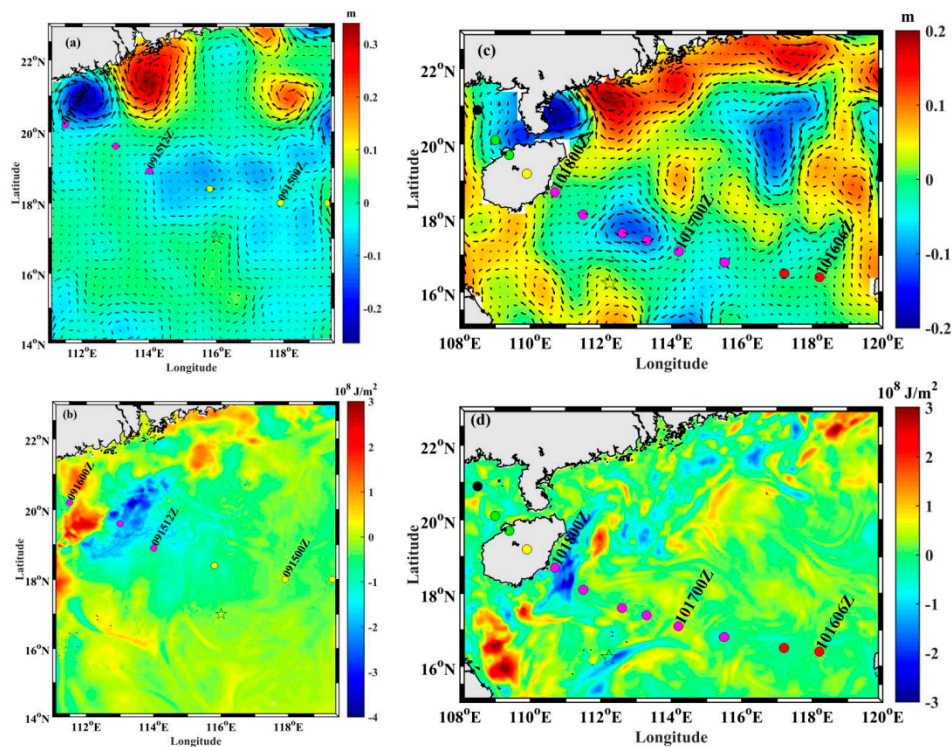
**Figure 5.** The altimeter-derived SSHA and GVA between post-storm and pre-storm conditions for: (**a**) Typhoon Kalmaegi; and (**c**) Typhoon Sarika. The color bar denotes SSHA variation in m. The ROMS-simulated OHC variations between post- and pre-storm conditions for: (**b**) Typhoon Kalmaegi; and (**d**) Typhoon Sarika. The color bar denotes the OHC variation in J/m$^2$. The black stars mark the position of the Argo floats. The colored circles mark the location of the typhoon center at different times, and the colors represent the maximum sustained wind speed (m/s): black for <20 m/s; green for 20–30 m/s; yellow for 30–35 m/s; magenta for 35–40 m/s; and red for >40 m/s.
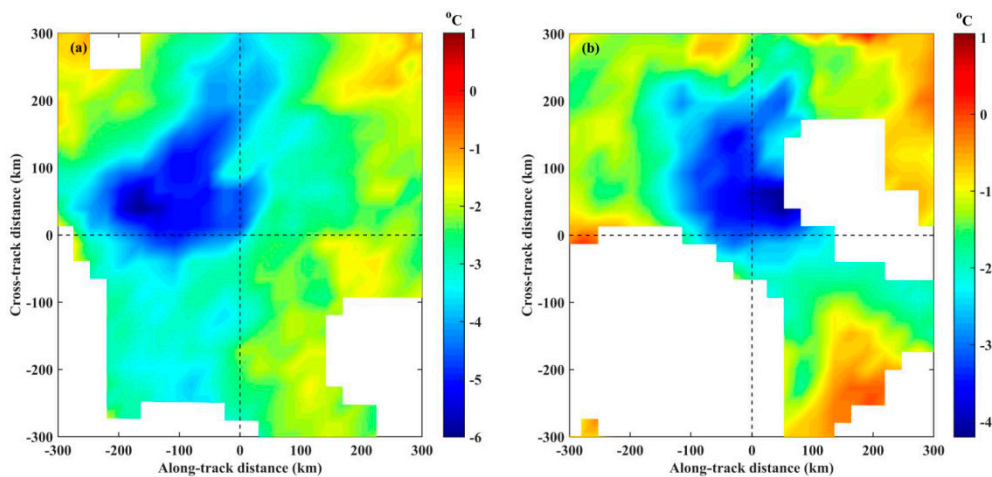


**Figure 6.** SST changes induced by Typhoons: (**a**) Kalmaegi; and (**b**) Sarika. The intersection of the dotted lines marks the location of the typhoon center, and the centers of the Typhoons Kalmaegi and Sarika are at 18.9°N, 114°E and 18.1°N, 111.5°E, and at 12:00 UTC on 15 September 2014 and at 18:00 UTC on 17 October 2016, respectively. The negative direction of the horizontal axis denotes the typhoon's translation direction. The top and bottom halves of the vertical axis represent the left and right sides of the typhoon track, respectively. The color bar denotes SST variation, in units of °C.

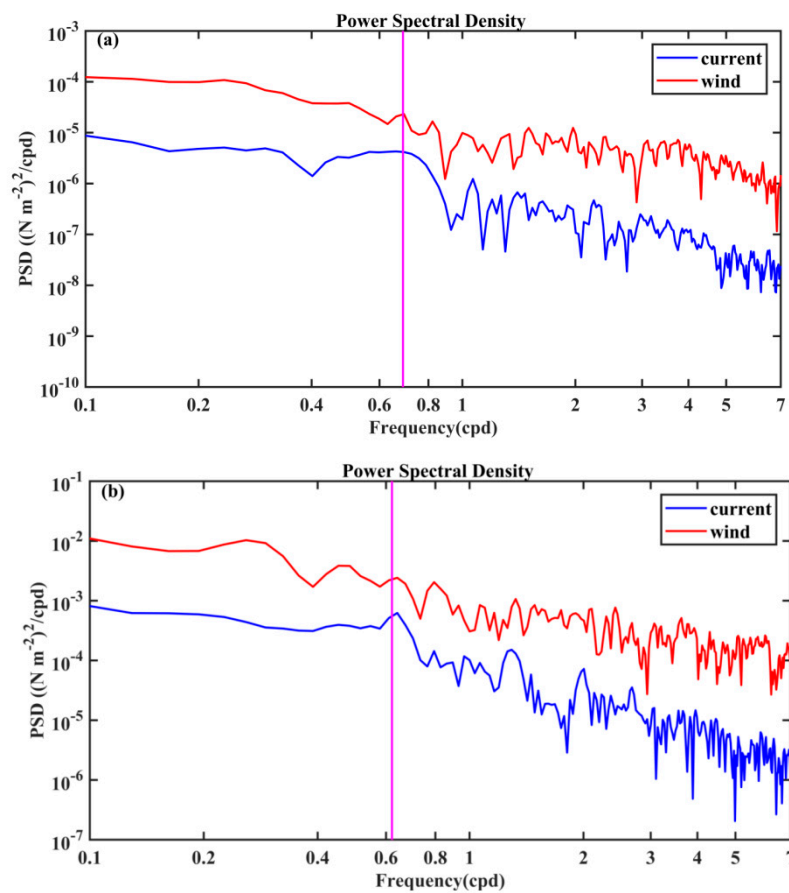**Figure 7.** PSD of the wind speed (red lines) and current speed (blue lines) for Typhoon: (**a**) Kalmaegi; and (**b**) Sarika. The magenta lines denote the near-inertial frequency.

We only used satellite observations to study SST response to typhoons. To investigate subsurface temperature responses, we analyzed vertical temperature changes measured by Argo floats before and during Typhoons Kalmaegi and Sarika, the results of which are shown in Figure 8. Figure 8b,d show a decrease of 0.1 °C–1.3 °C in the temperature above 95 m, and the depth of mixed layer was 36 m on 15 September 2014. The Argo-measured OHC decreases from $1.09 \times 10^8$ J/m$^2$ to $0.89 \times 10^8$ J/m$^2$. This suggests that the heat exchange at the air–sea interface and advection contribute to the upper ocean temperature cooling in the initial stage of typhoon forcing on 15 September 2014. Figure 8d shows the depth of mixed layer deepening from 36 m to 46 m on 19 September 2014. Four days after the passage of Typhoon Kalmaegi, there was a decrease of 0.4 °C–0.6 °C in the temperature above 36 m, but an increase of 0.1 °C–1.1 °C in the temperature between 36 m and 80 m. The mixing induced by Typhoon Kalmaegi plays an important role on the surface cooling and subsurface warming. Figure 8f reveals that Typhoon Sarika triggered a different subsurface temperature response than Typhoon Kalmaegi. The subsurface temperature response demonstrates a three-layer vertical structure, with a 0.8 °C–1.8 °C temperature decrease above 45 m, a 0.3 °C–1.5 °C increase between 45 m and 70 m, and a 0.6 °C–1.6 °C decrease between 70 m and 95 m. The OHC decreases from $1.41 \times 10^8$ J/m$^2$ to $0.86 \times 10^8$ J/m$^2$, and Figure 8h shows the mixed layer deepening by 20 m during the passage of Typhoon Sarika. Four days after Typhoon Sarika, SST recovered to 29.3 °C (SST was 29.6 °C before the typhoon), whereas the subsurface temperatures remained warm state. This was owing to the net heat input to the subsurface that was retained by mixing while the surface temperature gradually recovered. Many studies have shown that the "heat pump" effect is critical to global circulation and heat transport [9,10,44,45].
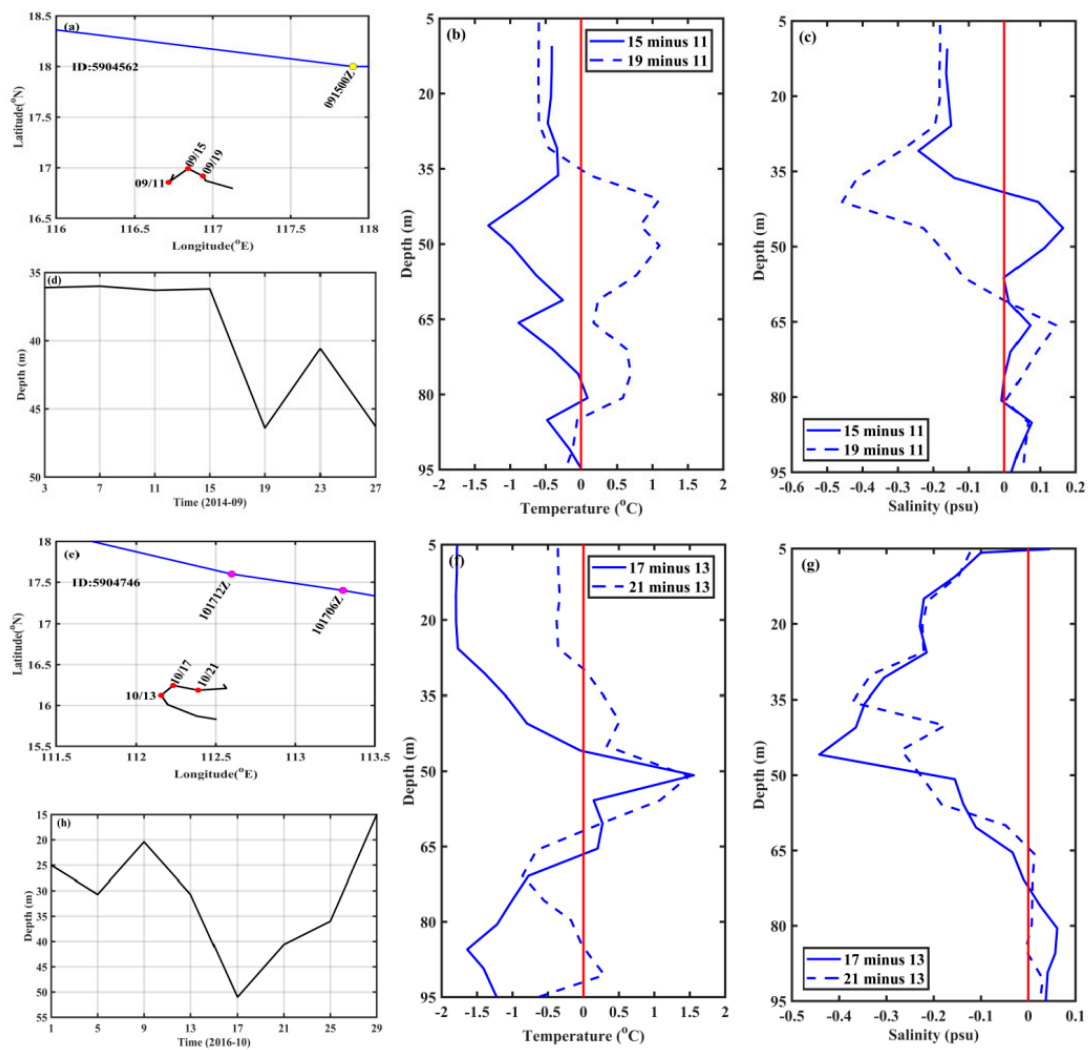
**Figure 8.** Vertical temperature and salinity measured by Argo floats at profiling interval of four days: (**a**) the tracks of Argo floats (black line); and (**e**) the locations of the profiles used in (**b**,**c**,**f**,**g**) (red dots). The blue line denoted the typhoon tracks, and the yellow and magenta dots denote the center of the typhoons. (**b**) Temperature; and (**c**) salinity differences on 11 September, 15 September, and 19 September 2014; and (**f**) temperature; and (**g**) salinity differences on 13 October, 17 October, and 21 October 2016. The blue solid lines denote the changes during the and before storm, the blue dashed lines denote the changes between the post- and pre-storm, and the red solid lines denote the zero line. The mixed layer depth measured by Argo float (**d**) 5904562 during Typhoon Kalmaegi (2014) (maximum sustained wind of 33.4 m/s) and (**h**) 5904746 during Typhoon Sarika (2016) (maximum sustained wind of 38.6 m/s).

Figure 9 shows CTD-measured and ROMS-simulated temperature evolutions for Typhoon Kalmaegi between 0 and 200 m depths at stations B2 and B4. Again, both in situ measurements and model simulations showed significant SST cooling and deepening of the mixed layer when the typhoon passed. ROMS-simulated SST changes before and during the passage of Typhoon Kalmaegi are shown in Figure 10. Compared to satellite observations (Figure 3c), the model-simulated SST cooling has a smaller amplitude than observations, a discrepancy that is largely linked to atmospheric forcing. Moreover, the stratification defined by the buoyancy frequency ($\overline{N}$) [19] is as follows,

$$\overline{N}^2 = -\frac{g}{\rho_0}\frac{\partial\overline{\rho}}{\partial z} \qquad (2)$$

where $g \approx 9.8$ m/s$^2$, $\rho$ is the potential density of seawater temperature and salinity at depth $z$. The ROMS-simulated maximum buoyancy frequency (MBP) occurred at 54.2 m ($\overline{N} = 4.9 \times 10^{-2}$ s$^{-1}$), whereas the CTD-measured MBP occurred at 39.2 m ($\overline{N} = 2.7 \times 10^{-2}$ s$^{-1}$). It is obvious that the ROMS-simulated buoyancy frequency is stronger than the CTD measurements, and the stronger stratification yields smaller SST cooling amplitude.
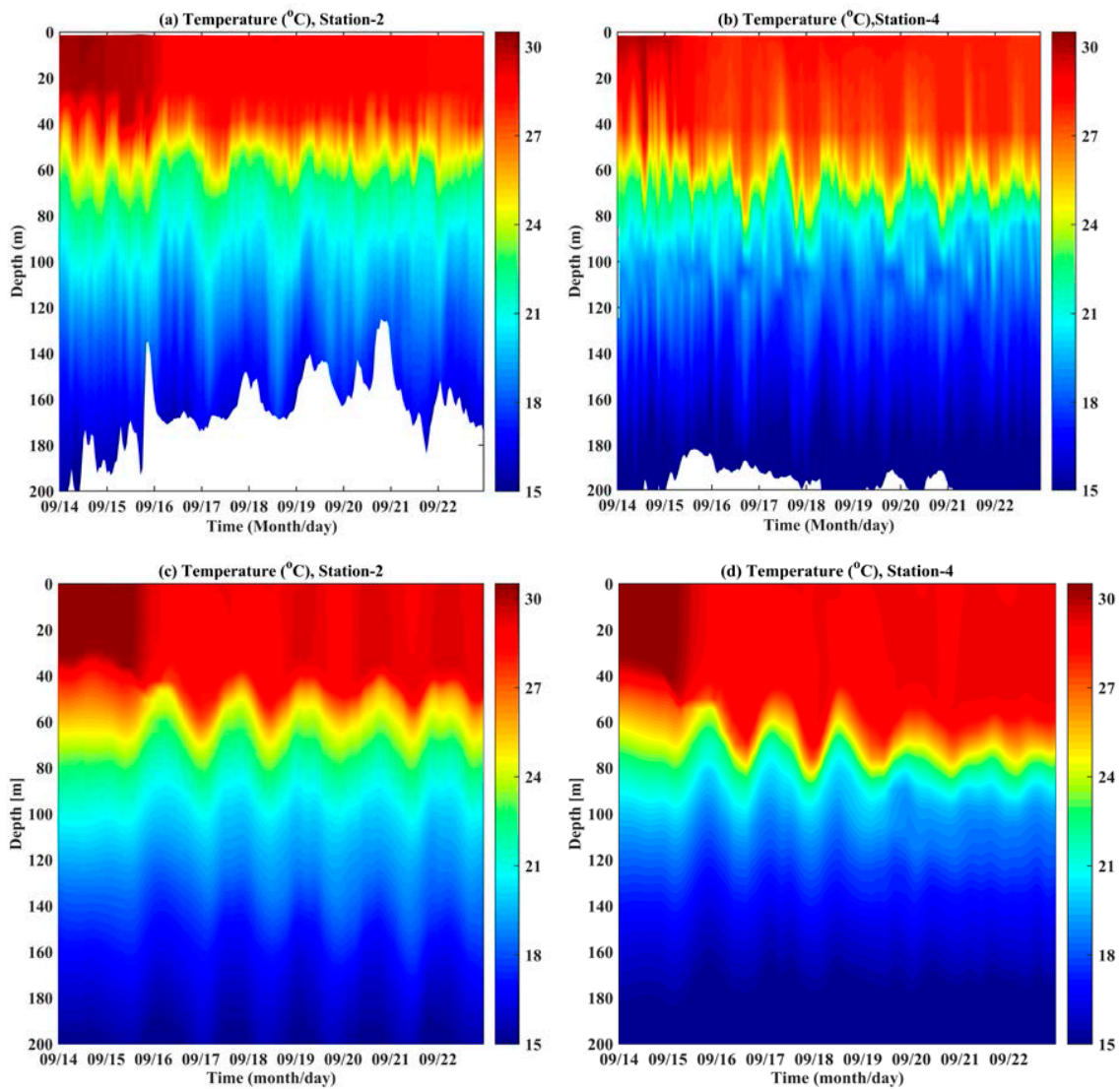


**Figure 9.** (**a**,**b**) CTD-measured temperatures from 0–200 m deep at two different stations; and (**c**,**d**) ROMS-simulated temperatures from 0–200 m deep at two different stations. The color bar denotes the temperature, in units of °C.
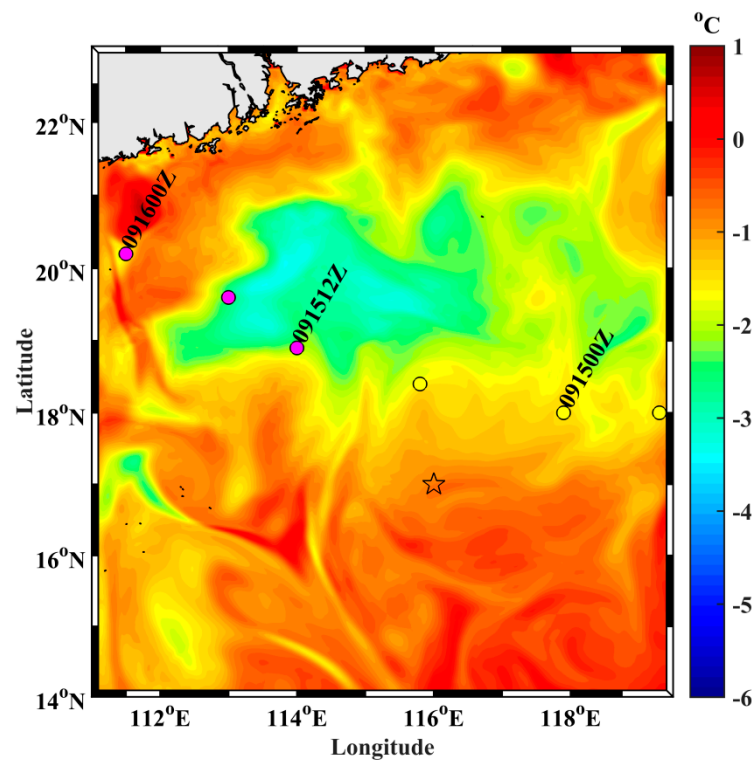
**Figure 10.** ROMS-simulated sea surface temperature differences between 16 September and 14 September 2014. The color bar denotes the temperature difference, in units of °C. The color circles show the location of the typhoon center at different times and the colors denote the maximum sustained wind speed (m/s): yellow for 31–35 m/s; magenta for 36–40 m/s.

*3.2. Salinity Response*

Figure 11 shows the SMAP Level 3 Running 8-day SSS maps before (Figure 11a), during (Figure 11b,c) and after (Figure 11d,e) Typhoon Sarika. Figure 11f illustrates typhoon-induced SSS changes. The maximum SSS increase was 2.2 psu to the right side of Typhoons Sarika's track, whereas the maximum salinity decrease was 1.4 psu to the left side. SSS was increased compared to pre-typhoon conditions on the right side because the wind stress vector rotates clockwise on the right side of the typhoon track and remains parallel with the inertially rotating mixed layer current. This results in strong vertical mixing, and thus, brings saltier water from the deep ocean to the surface. Figure 12 shows that high rainfall rates occurred on the left side of Typhoon Sarika's track. Many studies have shown that the remarkable asymmetric TC rainfall distribution is caused by the vertical wind shear, tropical cyclones motion, and water vapor flux or topography, in which the vertical wind shear is the primary factor [46–53]. Moreover, the rainfall maximum in the inner-core region of a TC is always located on the downshear left side for TCs in the Northern Hemisphere regardless of the storm motion and shear orientation [52,53]. The decreasing SSS on the left side was induced by intense rainfall injecting fresh water into the ocean. Moreover, the typhoon-induced SSS drop on the left side of the typhoon's track was also confirmed by Argo observations. The GPM-measured rainfall rate was 6.8 mm/h at the Argo position, which led to a salinity decrease of 0.02–0.41 psu above 70 m on the left side as shown in Figure 8g.
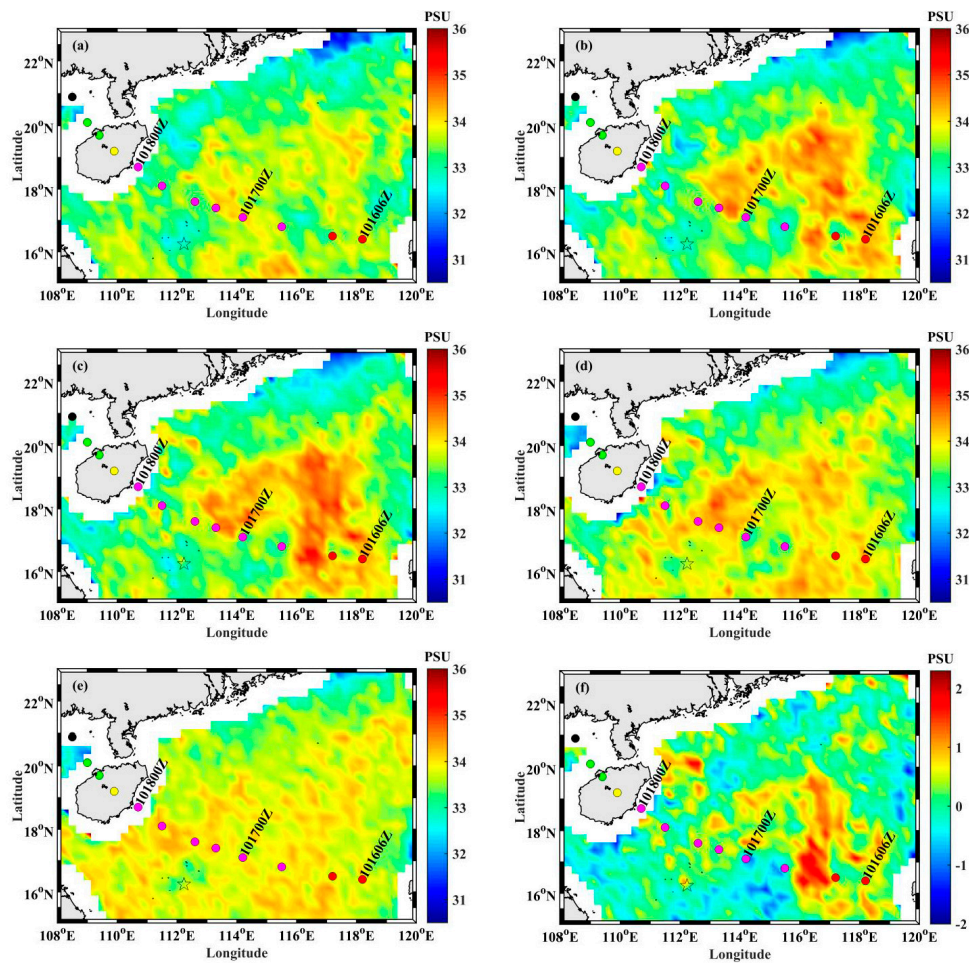
**Figure 11.** SMAP Level 3 8-day Running sea surface salinity (SSS) data showing the SSS as Typhoon Sarika passed: (**a**) on 11 October 2016; (**b**) on 14 October 2016; (**c**) on 17 October 2016; (**d**) on 20 October 2016; (**e**) and on 23 October 2016. (**f**) SSS difference between 17 October and 11 October 2016. The color bar denotes the salinity, in units of PSU. The colored circles denote the location of the typhoon center at different times and the colors denote the maximum sustained wind speed (m/s): black for <20 m/s; green for 20–30 m/s; yellow for 30–35 m/s; magenta for 35–40 m/s; and red for >40 m/s. The black star marks the position of Argo float 5904746.

Salinity profiles from CTD observations and ROMS simulations, are illustrated in Figure 13, both revealed that subsurface salinity increased at stations B2 and B4 during Typhoon Kalmaegi. The CTD measurements clearly showed maximum salinity increases in the subsurface layer at stations B2 and B4 of 0.32 and 0.17 psu, respectively (Figure 13a,b). ROMS simulations also exhibited subsurface salinity increases at the two stations, with respective values of 0.39 and 0.26 psu, as shown in Figure 14c,d. The CSFv2-derived rainfall rates at stations B2 and B4 were 4.6 mm/h and 2.6 mm/h, while the WindSat-measured rainfall rates were 6.5 mm/h and 4.3 mm/h. Model-simulated salinity maxima are slightly higher than those measured by CTD, which is possibly associated with the lower CSFv2-derived rainfall rate for the model input. Moreover, Argo salinity profile measurements also confirm that subsurface salinity increased by up to 0.16 psu between 40 m and 100 m, as shown in Figure 8c. The rainfall rate was 12 mm/h in the Argo position (Figure 14), resulting in a salinity decrease of 0.14–0.24 psu above 40 m.
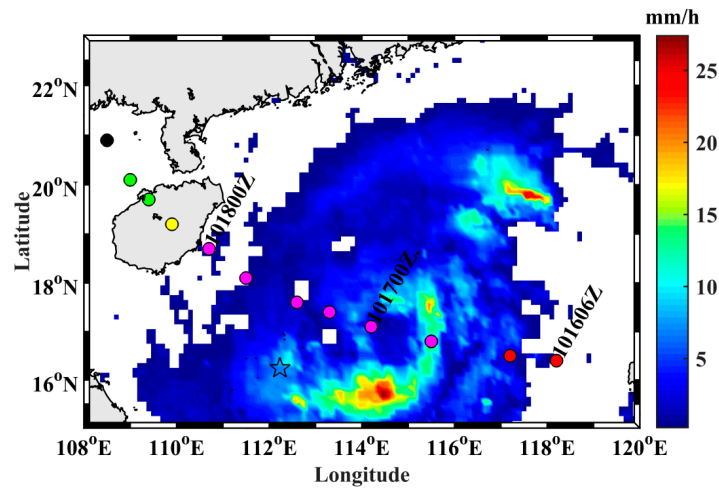
**Figure 12.** GPM-measured rain rates at 00:00 UTC on 17 October 2016. The color bar denotes rainfall rate in mm/h. White indicates no rain. The black star denotes the position of Argo float 5904746. The colored circles show the location of the typhoon center at different times and the colors represent the maximum sustained wind speed (m/s): black for <20 m/s; green for 20–30 m/s; yellow for 30–35 m/s; magenta for 35–40 m/s; and red for >40 m/s.
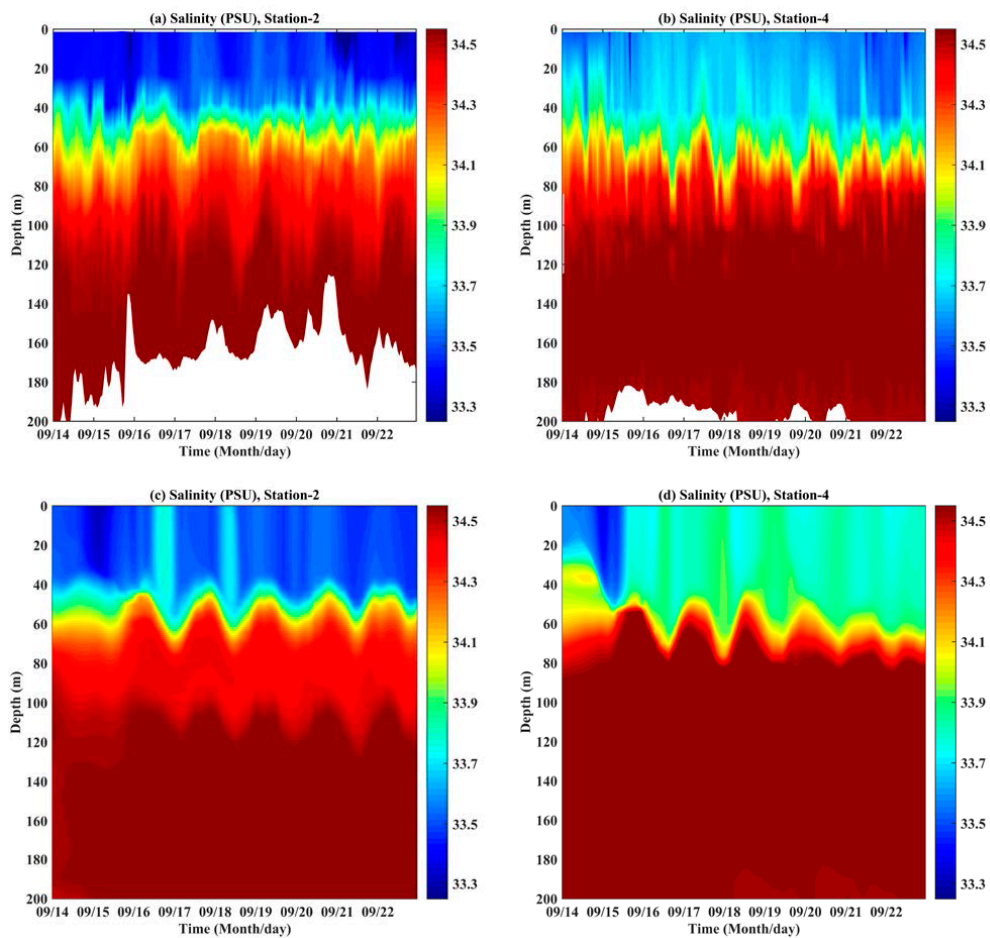


**Figure 13.** (**a**,**b**) CTD-measured salinity at 0–200 m deep at two different stations; and (**c**,**d**) ROMS-simulated salinity at 0–200 m deep at two different stations. The color bar denotes the salinity, in units of PSU.
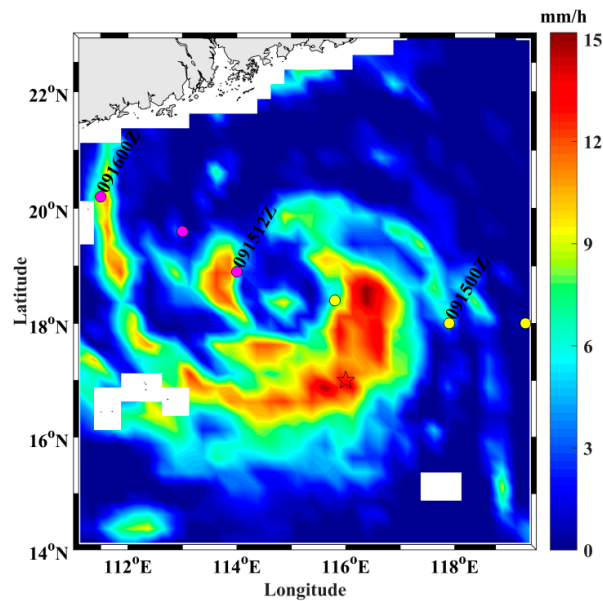
**Figure 14.** WindSat-measured rainfall rates at 10:12 UTC on 15 September 2014. The color bar denotes rainfall rate in mm/h. The black star denotes the position of Argo float 5904562. The colored circles show the location of the typhoon center at different times and the colors denote the maximum sustained wind speed (m/s): yellow for 31–35 m/s; magenta for 36–40 m/s.

### 3.3. Current Response

Strong typhoon-forced winds can enhance near-surface ocean current velocity. Ocean current response to Typhoon Kalmaegi was clearly observed by ADCP at stations B1, B2, and B4, as shown in Figure 15a–c. B1 and B4 stations were on the right side of Typhoon Kalmaegi's track and B2 was on the left. Before Typhoon Kalmaegi's arrival, ADCP-measured current velocity maxima were 0.5 m/s at B1, 0.3 m/s at B2, and 0.4 m/s at B4, occurring depths of 30, 14, and 22 m, respectively. During Typhoon Kalmaegi's passage, the current velocity maxima measured at the same depths increased to 1.18, 0.86, and 1.19 m/s, respectively. The ADCP-measured subsurface current velocities at stations B1 and B4 are stronger than those measured at B2 because the wind stress is better coupled with the inertial currents on the right side than that those to the left side. After Typhoon Kalmaegi passed, the maximum current velocities were 1.22, 1.01, and 1.23 m/s at stations B1, B2, and B4, at depths of 54, 46, and 94 m, respectively. It is indicated that the mixed layer depth was deepened, which was mainly caused by near-inertial current shear at the base of the mixed layer.

We also used a ROMS model to simulate surface and subsurface current responses to typhoons. Figure 15d–f shows model-simulated current velocities at stations B1, B2, and B4. This demonstrates that model simulations can reproduce ADCP-observed current response characteristics well. Maximum current velocities from ROMS model simulation were 1.49 m/s at station B1, 1.23 m/s at station B2, and 1.41 m/s at station B4, respectively. Generally, the large wind stresses lead to strong ocean current. This drag coefficient in the COARE3.0 algorithm is larger than that used in [54] for high wind speeds. Therefore, it might cause that the model-simulated current velocities are larger than those from ADCP measurements. Moreover, Figure 16 shows near-surface current velocity differences, from the ROMS simulation, before and during Typhoon Kalmaegi passes. This demonstrates that current velocity changes also presented a rightward bias; current velocities on the right side of typhoon track are higher than on the left.
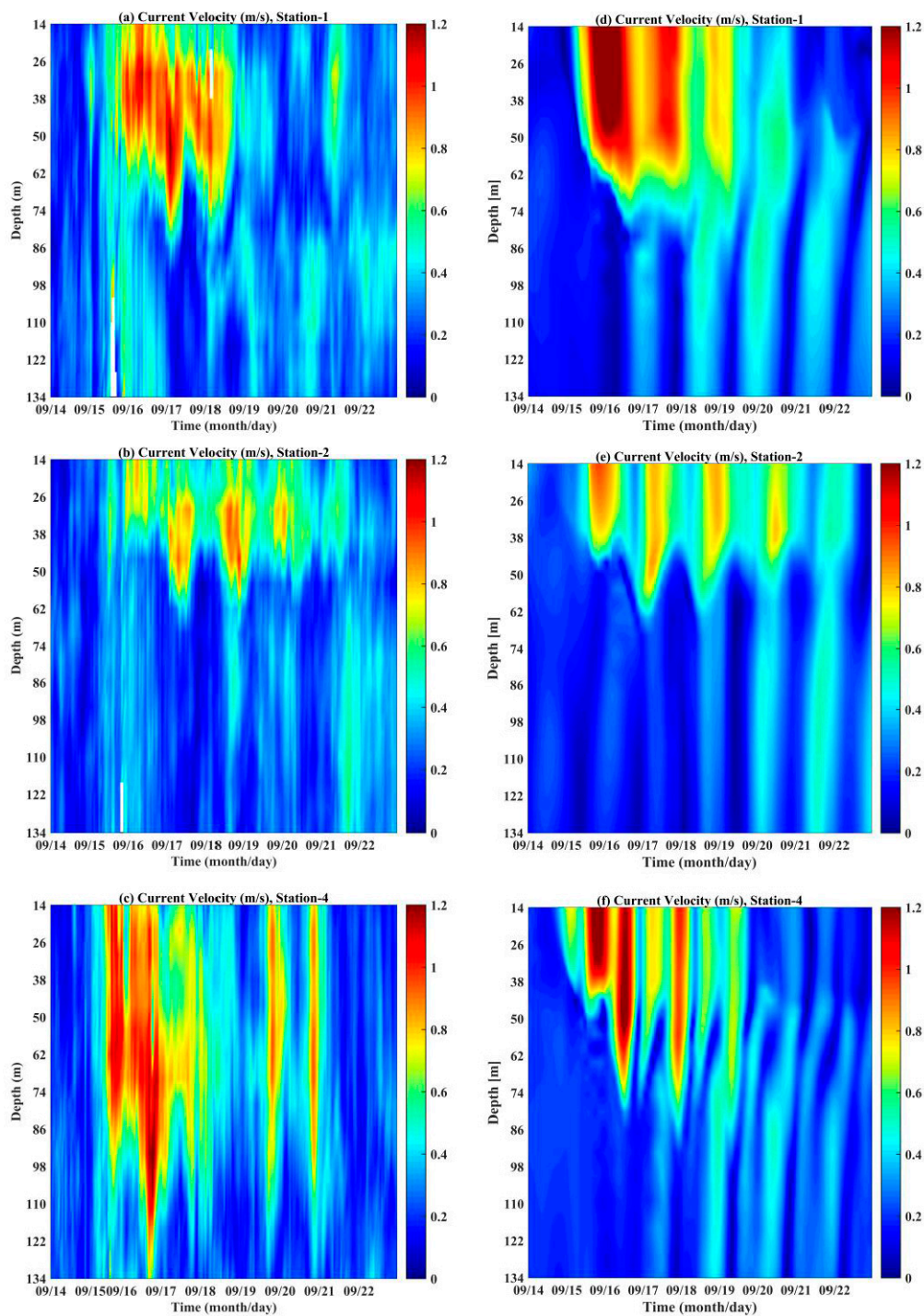
**Figure 15.** Time series of current velocity profiles observed by ADCP at: (**a**) station B1; (**b**) station B2; and (**c**) station B4 during the passage of Typhoon Kalmaegi. Time series of current velocity profiles simulated by the ROMS at: (**d**) station B1; (**e**) station B2; and (**f**) station B4 during the passage of Typhoon Kalmaegi. The color bar denotes the current velocity, in units of m/s.
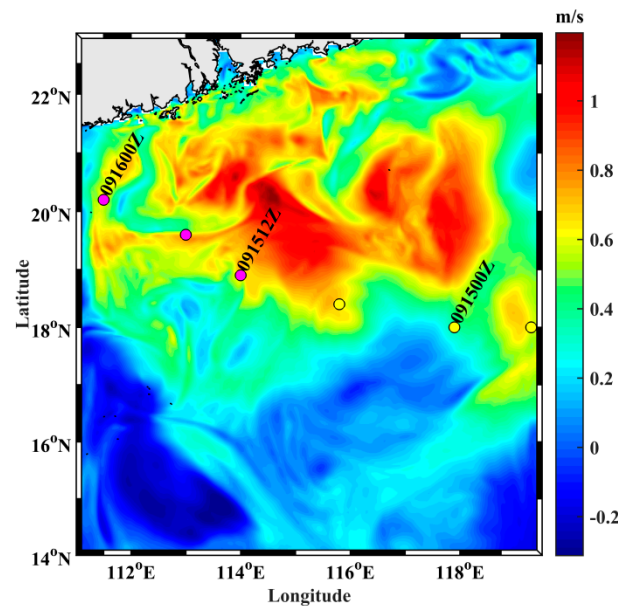
**Figure 16.** ROMS-simulated near-surface current velocity difference between 15 September and 14 September 2014. The color bar denotes the current velocity difference, in units of m/s. The colored circles denote the location of the typhoon center at different times and the colors denote the maximum sustained wind speed (m/s): yellow for 31–35 m/s; magenta for 36–40 m/s.

## 4. Conclusions

We quantified physical responses of the ocean surface to Typhoons Kalmaegi and Sarika, based on multi-satellite observations, in situ measurements, and a numerical ocean model. Using satellite observations and ocean simulations, we confirmed that strong typhoon winds pumped cold and salty deep waters from the mixed layer to the sea surface, which resulted SST cooling and SSS increases. Typhoon force winds induced strong vertical mixing and upwelling, leading to enhanced near-surface ocean currents. SST and current responses both exhibited obvious rightward biases because of the rotation resonance of the wind vector with wind-driven inertial currents.

The maximum amplitudes of SST decrease were 6 °C and 4.2 °C for Typhoons Kalmaegi and Sarika, respectively. Regarding Typhoon Sarika, measurements from Argo temperature profiles showed that the subsurface temperature response had a three-layer vertical structure, with a 0.8 °C–1.8 °C temperature decrease above 45 m, a 0.3 °C–1.5 °C increase between 45 m and 70 m, and a 0.6 °C–1.6 °C decrease between 70 m and 95 m. After Typhoon Sarika passed, SST recovered to their pre-typhoon condition, whereas subsurface temperatures remained in a warm state. This is due to the net heat input to the subsurface that is retained by mixing, while the surface temperature gradually recovers. Many studies have shown that the "heat pump" effect have important effects on the global circulation and the heat transport [9,10,44,45].

SMAP Level 3 8-day Running SSS maps show that the maximum SSS increase was 2.2 psu on the right side of Typhoon Sarika's track, whereas the maximum salinity decrease was 1.4 psu on the left. This SSS seesaw response phenomenon is related to asymmetrical rainfall on both sides of the typhoon track. SSS on the right side was higher than pre-typhoon conditions because typhoon-induced vertical mixing brings saltier deep water to the surface. Decreasing SSS on the left side is induced by intense rainfall injecting fresh water into the ocean. Moreover, Argo salinity profile measurements also confirmed the left side SSS decrease.

Both numerical simulations and ADCP observations revealed upper ocean current response to typhoons. When Typhoon Kalmaegi passed, the highest current velocities measured by ADCP at depths of 30, 14, and 22 m, were 1.18, 0.86, and 1.19 m/s, respectively. After Typhoon Kalmaegi

passed, the maximum current velocities were 1.22, 1.01, and 1.23 m/s at stations B1, B2, and B4, with corresponding depths of 54, 46, and 94 m. It is indicated that the mixed layer depth was deepened, which was mainly caused by near-inertial current shear at the base of the mixed layer.

Factors such as accurate atmospheric forcing fields, suitable drag coefficient under high wind speed, vertical parameterization schemes, and the reason to use coupled ocean–atmosphere models, depending on the condition will directly affect the simulation results. Furthermore, we will use the wind field of high-resolution microwave radiometers to provide atmospheric forcing and study ocean response before, during, and after the passage of a typhoon. We will further analyze the physical mechanism of the changes in detail using the simulation results, including the roles of entrainment, KPP mixing, and upwelling.

**Author Contributions:** Biao Zhang and Guoqiang Liu conceived the original idea of the study, suggested for the topic, and contributed to the interpretation of the results; Xinxin Yue carried out satellite data analysis, numerical simulations and prepared all of the figures; Han Zhang processed and analyzed in situ data; Xiaofeng Li and Yijun He assisted in manuscript preparation and revision. Xinxin Yue and Biao Zhang wrote the manuscript.

**Conflicts of Interest:** The authors declare no conflict of interest.

## References

1. Knustson, T.R.; McBride, J.L.; Chan, J.; Emanuel, K.; Holland, G.; Landsea, C.; Held, I.; Kossin, J.P.; Srivastava, A.K.; Sugi, M. Tropical cyclones and climate change. *Nat. Geosci.* **2010**, *3*, 157–163. [CrossRef]
2. Walsh, K.J.E.; McBride, J.L.; Klotzbach, P.J.; Balachandran, S.; Camargo, S.J.; Holland, G.; Knutson, T.R.; Kossin, J.P.; Lee, T.; Sobel, A.; et al. Tropical cyclones and climate change. *WIREs Clim. Chang.* **2016**, *7*, 65–89. [CrossRef]
3. Webster, P.J.; Holland, G.J.; Curry, J.A.; Chang, H.-R. Changes in Tropical Cyclone Number, Duration, and Intensity in a Warming Environment. *Science* **2005**, *309*, 1844–1846. [CrossRef] [PubMed]
4. Emanuel, K. Increasing destructiveness of tropical cyclones over the past 30 years. *Nature* **2005**, *436*, 686–688. [CrossRef] [PubMed]
5. Zhang, Q.; Liu, Q.; Wu, L. Tropical Cyclone Damages in China 1983-2006. *B. Am. Meteorol. Soc.* **2009**, *90*, 489–495. [CrossRef]
6. Price, J.F.; Sanford, T.B.; Forristall, G.Z. Forced stage response to a moving hurricane. *J. Phys. Oceanogr.* **1994**, *24*, 233–260. [CrossRef]
7. Price, J.F. Upper ocean response to a Hurricane. *J. Phys. Oceanogr.* **1981**, *11*, 153–175. [CrossRef]
8. Cornillon, P.; Stramma, L.; Price, J.F. Satellite measurements of sea surface cooling during hurricane Gloria. *Nature* **1987**, *326*, 373–375. [CrossRef]
9. Emanuel, K. Contribution of tropical cyclones to meridional heat transport by the oceans. *J. Geophys. Res. Atmos.* **2001**, *106*, 14771–14781. [CrossRef]
10. Sriver, R.L.; Huber, M. Observational evidence for an ocean heat pump induced by tropical cyclones. *Nature* **2007**, *447*, 577–580. [CrossRef] [PubMed]
11. Cheng, L.; Zhu, J.; Sriver, R.L. Global representation of tropical cyclone-induced short-term ocean thermal changes using Argo data. *Ocean Sci.* **2015**, *11*, 2831–2878. [CrossRef]
12. Lin, I.; Liu, W.T.; Wu, C.-C.; Wong, G.T.F.; Hu, C.; Zhen, Z.; Liang, W.-D.; Yang, Y.; Liu, K.-K. New evidence for enhanced ocean primary production triggered by tropical cyclone. *Geophys. Res. Lett.* **2003**, *30*, 1718. [CrossRef]

13. Shang, S.; Li, L.; Sun, F.; Wu, J.; Hu, C.; Chen, D.; Ning, X.; Qiu, Y.; Zhang, C.; Shang, S. Changes of temperature and bio-optical properties in the South China Sea in response to Typhoon Lingling, 2001. *Geophys. Res. Lett.* **2008**, *35*, L10602. [CrossRef]

14. Stramma, L.; Cornillon, P.; Price, J.F. Satellite observations of sea surface cooling by hurricanes. *J. Geophys. Res. Oceans* **1986**, *91*, 5031–5035. [CrossRef]

15. Wei, W.; Lien, C.-C.; Lin, I.-I.; Xie, S.-P. Tropical Cyclone-Induced Ocean Response: A Comparative Study of the South China Sea and Tropical Northwest Pacific. *J. Clim.* **2015**, *28*, 5952–5968.

16. Knaff, J.A.; DeMaria, M.; Sampson, C.R.; Peak, J.E.; Cummings, J.; Schubert, W.H. Upper oceanic energy response to tropical cyclone passage. *J. Clim.* **2013**, *26*, 2631–2650. [CrossRef]

17. Mei, W.; Pasquero, C. Restratification of the upper ocean after the passage of a tropical cyclone: A numerical study. *J. Phys. Oceanogr.* **2012**, *42*, 1377–1401. [CrossRef]

18. Park, J.J.; Kwon, Y.; Price, J.F. Argo array observation of ocean heat content changes induced by tropical cyclones in the north Pacific. *J. Geophys. Res. Oceans* **2011**, *116*. [CrossRef]

19. Shay, L.K.; Goni, G.J.; Black, P.G. Effects of a Warm Oceanic Feature on Hurricane Opal. *Mon. Weather Rev.* **2000**, *128*, 1366–1383. [CrossRef]

20. Lin, I.I.; Wu, C.C.; Emanuel, K.A.; Lee, I.-H.; Wu, C.-R.; Pun, I.-F. The Interaction of Supertyphoon Maemi (2003) with a Warm Ocean Eddy. *Mon. Weather Rev.* **2005**, *133*, 2635–2649. [CrossRef]

21. Domingues, R.; Goni, G.; Bringas, F.; Lee, S.-K.; Kim, H.-S.; Halliwell, G.; Dong, J.; Morell, J.; Pomales, L. Upper ocean response to Hurricane Gonzalo (2014): Salinity effects revealed by targeted and sustained underwater glider observations. *Geophys. Res. Lett.* **2015**, *42*, 7131–7138. [CrossRef]

22. Yan, Y.; Li, L.; Wang, C. The effects of oceanic barrier layer on the upper ocean response to tropical cyclones. *J. Geophys. Res. Oceans* **2017**, *122*, 4829–4844. [CrossRef]

23. Chang, Y.C.; Chen, G.Y.; Tseng, R.S.; Centurioni, L.R.; Chu, P.C. Observed near-surface flows under all tropical cyclone intensity levels using drifters in the northwestern Pacific. *J. Geophys. Res. Oceans* **2013**, *118*, 2367–2377. [CrossRef]

24. Chang, Y.C.; Chu, P.C.; Centurioni, L.R.; Tseng, R.S. Observed near-surface currents under four super typhoons. *J. Mar. Syst.* **2014**, *139*, 311–319. [CrossRef]

25. Shen, J.; Qiu, Y.; Zhang, S.; Kuang, F. Observation of Tropical Cyclone Induced Shallow Water Currents in Taiwan Strait. *J. Geophys. Res. Oceans* **2017**, *122*, 5005–5021. [CrossRef]

26. Rayson, M.D.; Ivey, G.N.; Jones, N.L.; Lowe, R.J.; Wake, G.W.; McConochie, J.D. Near-inertial ocean response to tropical cyclone forcing on the Australian North-West Shelf. *J. Geophys. Res. Oceans* **2015**, *120*, 7722–7751. [CrossRef]

27. Zhang, H.; Chen, D.; Zhou, L.; Liu, X.; Ding, T.; Zhou, B. Upper ocean response to typhoon Kalmaegi (2014). *J. Geophys. Res. Oceans* **2016**, *121*, 6520–6535. [CrossRef]

28. Sun, Y.; Pan, J.; Perrie, W. Upper Ocean Physical and Biological Response to Typhoon Cimaron (2006) in the South China Sea. In *Recent Development in Tropical Cyclone Dynamics, Prediction, and Detection*; Lupo, A.R., Ed.; InTechOpen: London, UK, 2016; pp. 67–87.

29. Shay, L.K.; Black, P.G.; Mariano, A.J.; Hawkins, J.D.; Elsberry, R.L. Upper ocean response to Hurricane Gilbert. *J. Geophys. Res.* **1992**, *97*, 20227–20248. [CrossRef]

30. Hormann, V.L.; Centurioni, R.; Rainville, L.; Lee, C.M.; Braasch, L.J. Response of upper ocean currents to Typhoon Fanapi. *Geophys. Res. Lett.* **2014**, *41*, 3995–4003. [CrossRef]

31. Liu, Z.; Xu, J.; Sun, C.; Wu, X. An upper ocean response to typhoon Bolaven analyzed with Argo profiling floats. *Acta Oceanol. Sin.* **2014**, *33*, 90–101. [CrossRef]

32. Lin, S.; Zhang, W.; Shang, S.; Hong, H. Ocean response to typhoons in the western North Pacific: Composite results from Argo data. *Deep-Sea Res. I* **2017**, *123*, 62–74. [CrossRef]

33. Meissner, T.; Wentz, F.J. Remote Sensing Systems SMAP Ocean Surface Salinities [Level 2C, Level 3 Running 8-day, Level 3 Monthly]. 2016, Version 2.0 Validated Release. Remote Sensing Systems, Santa Rosa, CA, USA. Available online: www.remss.com/missions/smap (accessed on 19 February 2018).

34. Shchepetkin, A.F.; McWilliams, J.C. The regional oceanic modeling system: A split-explicit, free-surface, topography-following-coordinate ocean model. *Ocean Model.* **2005**, *9*, 347–404. [CrossRef]

35. Haidvogel, D.; Arango, H.; Budgell, W.P. Ocean forecasting in terrain-following coordinates: Formulation and skill assessment of the Regional Ocean Modeling System. *J. Comput. Phys.* **2008**, *227*, 3595–3624. [CrossRef]

36. Haidvogel, D.B.; Arango, H.G.; Hedstrom, K.; Beckmann, A.; Malanotte-Rizzoil, P.; Shchepetkin, A.F. Model Evaluation Experiments in the North Atlantic Basin: Simulations in Nonlinear Terrian-Following Coordinates. *Dyn. Atmos. Oceans* **2000**, *32*, 239–281. [CrossRef]

37. Fairall, C.W.; Bradley, E.F.; Rogers, D.P.; Edson, J.B.; Young, G.S. Bulk parameterization of air-sea fluxes for Tropical Ocean-Global Atmosphere Coupled-Ocean Atmosphere Response Experiment. *J. Geophys. Res.* **1996**, *101*, 3747–3764. [CrossRef]

38. Fairall, C.W.; Bradley, E.F.; Hare, J.E.; Grachev, A.A.; Edson, J.B. Bulk parameterization of air-sea fluxes: Updates and verification for the COARE algorithm. *J. Clim.* **2003**, *16*, 571–591. [CrossRef]

39. Large, W.G.; McDougall, T.J.; Dongy, S.C. Oceanic vertical mixing: a review and a model with a nonlocal boundary layer parameterization. *Rev. Geophys.* **1994**, *32*, 363–403. [CrossRef]

40. Jacob, S.D.; Shay, L.K. The role of oceanic mesoscale features on the tropical cyclone-induced mixed layer response: A case study. *J. Phys. Oceanogr.* **2003**, *33*, 649–676. [CrossRef]

41. Saha, S.; Moorthi, S.; Wu, X.; Wang, J.; Nadiga, S.; Tripp, P.; Behringer, D.; Hou, Y.T.; Chuang, H.; Iredell, M.; et al. The NCEP Climate Forecast System Version 2. *J. Clim.* **2014**, *27*, 2185–2208. [CrossRef]

42. Chassignet, E.P.; Hurlburt, H.E.; Smedstad, O.M.; Halliwell, G.R.; Hogan, P.J.; Wallcraft, A.J.; Baraille, R.; Bleck, R. The HYCOM (HYbrid Coordinate Ocean Model) data assimilative system. *J. Mar. Syst.* **2007**, *65*, 60–83. [CrossRef]

43. Cheung, H.F.; Pan, J.; Gu, Y.; Wang, Z. Remote sensing observation of ocean responses to Typhoon Lupit in the northwest Pacific. *Int. J. Remote Sens.* **2013**, *34*, 1478–1491. [CrossRef]

44. Korty, R.L.; Emanuel, K.A.; Scott, J.R. Tropical cyclone-induced upper-ocean mixing and climate: Application to equable climates. *J. Clim.* **2008**, *21*, 638–654. [CrossRef]

45. Pasquero, C.; Emanuel, K. Tropical cyclones and transient upper-ocean warming. *J. Clim.* **2008**, *21*, 149–162. [CrossRef]

46. Burpee, R.W.; Black, M.L. Temporal and spatial variations of rainfall near the centers of two tropical cyclones. *Mon. Weather Rev.* **1989**, *117*, 2204–2218. [CrossRef]

47. Corbosiero, K.L.; Molinari, J. The relationship between storm motion, vertical wind shear, and convective asymmetries in tropical cyclones. *J. Atmos. Sci.* **2003**, *60*, 366–376. [CrossRef]

48. Chen, L.S.; Li, Y.; Cheng, Z.Q. An overview of research and forecasting on rainfall associated with landfalling tropical cyclones. *Adv. Atmos. Sci.* **2010**, *27*, 967–976. [CrossRef]

49. Chen, S.S.; Knaff, J.A.; Marks, F.D. Effects of vertical wind shear and storm motion on tropical cyclone rainfall asymmetries deduced from TRMM. *Mon. Weather Rev.* **2006**, *134*, 3190–3208. [CrossRef]

50. Xu, W.; Jiang, H.; Kang, X. Rainfall asymmetries of tropical cyclones prior to, during, and after making landfall in South China and Southeast. *Atmos. Res.* **2014**, *193*, 18–26. [CrossRef]

51. Yue, C.; Gao, S.; Liu, L.; Li, X. A diagnostic study of the asymmetric distribution of rainfall during the landfall of Typhoon Haitang. *Adv. Atmos. Sci.* **2015**, *32*, 1419–1430. [CrossRef]

52. Gao, S.; Zhai, S.; Li, T.; Chen, Z. On the asymmetric distribution of shear-relative typhoon rainfall. *Meteorol. Atmos. Phys.* **2018**, *130*, 11–22. [CrossRef]

53. Ueno, M. Observational Analysis and Numerical Evaluation of the Effects of Vertical Wind Shear on the Rainfall Asymmetry in the Typhoon Inner-Core Region. *J. Meteorol. Soc. Jpn.* **2007**, *85*, 115–136. [CrossRef]

54. Jaimes, B.; Shay, L.K.; Uhlhorn, E.W. Enthalpy and momentum fluxes during Hurricane Earl relative to underlying ocean features. *Mon. Weather Rev.* **2015**, *143*, 111–131. [CrossRef]